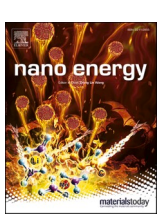
ELSEVIER

Contents lists available at ScienceDirect

Nano Energy

journal homepage: www.elsevier.com/locate/nanoen





Synergy of carbonyl and azo chemistries for wide-temperature-range rechargeable aluminum organic batteries

Kaiqiang Qin ^{a,1}, Sha Tan ^{b,1}, Motahareh Mohammadiroudbari ^a, Zhenzhen Yang ^c, Xiao-Qing Yang ^b, Enyuan Hu ^{b,*}, Chao Luo ^{a,d,**}

- ^a Department of Chemistry and Biochemistry, George Mason University, Fairfax, VA, 22030, USA
- b Chemistry Division, Brookhaven National Laboratory, Upton, NY 11973, USA
- ^c Chemical Sciences and Engineering Division, Argonne National Laboratory, Lemont, IL, 60439, USA
- ^d Quantum Science & Engineering Center, George Mason University, Fairfax, VA, 22030, USA

ARTICLE INFO

Keywords: Rechargeable aluminum batteries Redox-active polymer Cathode Wide temperature range Carbonyl group Azo group

ABSTRACT

Rechargeable aluminum organic batteries (RAOBs) are promising for developing cost-effective and sustainable energy storage devices due to the low cost, abundance, and high sustainability of aluminum and organic resources. Here, we designed and synthesized a redox-active polymer bearing carbonyl and azo groups as a cathode material for RAOBs. The polymeric cathode exhibits a high reversible specific capacity, superior cyclic stability, fast charging capability, and a wide operation temperature range (-40° C to 100° C). X-ray photoelectron spectroscopy (XPS), pair distribution function (PDF) analysis, and soft X-ray absorption near edge structure (XANES) were employed to gain fundamental insight into the carbonyl and azo chemistries in RAOBs, as well as the cathode electrolyte interphase (CEI) structure. We demonstrated a step-by-step alumination/de-alumination reaction for carbonyl and azo groups in the polymer cathode and unraveled a Al₂O₃- and AlN-rich CEI, which is critical for the impressive performance of RAOBs.

1. Introduction

Due to the ever-increasing demand for carbon neutrality and high sustainability, the development of sustainable and environmentally benign energy storage devices for portable electronics, electric vehicles, and grid-scale stationary energy storage is critical [1-4]. However, state-of-the-art Li ion batteries (LIBs) suffer from high cost, limited availability, and unevenly distribution of Li resources and transition-metal-based inorganic electrode materials [5-7]. Among various emerging battery systems beyond LIBs, rechargeable aluminum batteries (RABs) stand out because of the high theoretical capacity (2980 mAh g^{-1} or 8056 mAh cm⁻³ on account of Al/Al³⁺), low cost, abundance (the third most abundant element in the Earth's crust), high sustainability, and high safety of Al resources [8-12]. To achieve high-performance RABs, developing cathode materials that can reversibly store and release Al (complex) ions is pivotal. To date, carbon materials (graphite, graphene) and metal-based inorganic materials (metal sulfides, metal selenides, and metal oxides) are the commonly used cathode materials in RABs, which exhibit reversible storage of AlCl_4 ions or Al^{3+} ions [13–16]. Although the carbon materials deliver excellent electrochemical performance such as high working voltage, long lifetime, and superior rate capability, the capacity is restricted due to the limited lattice space to store AlCl_4 ions [17–19]. In addition, the strong Coulombic interaction between Al^{3+} ions and active host materials, as well as the high diffusion energy barrier of Al^{3+} ions hinder the ion diffusion in metal-based inorganic materials, resulting in sluggish reaction kinetics and poor cyclic stability [20–22]. Therefore, it is paramount to develop advanced cathode materials for high-capacity, high-rate, and stable RABs.

As universal electrode materials, organic materials including small organic molecules and redox-active polymers display high redox potentials and fast reaction kinetics in rechargeable aluminum organic batteries (RAOBs) because of their reversible redox nature and sufficient intermolecular space to form metal-ligand complexes with small Al complex carrier ions (such as $AlCl^{2+}$ or $AlCl^{2+}$) [23–26]. Compared with small organic molecules, redox-active polymers display significant

^{*} Corresponding author.

^{**} Corresponding author at: Department of Chemistry and Biochemistry, George Mason University, Fairfax, VA, 22030, USA. *E-mail addresses*: enhu@bnl.gov (E. Hu), cluo@gmu.edu (C. Luo).

¹ These authors contribute to this work equally

advantages such as negligible solubility in the electrolytes and flexible structures for accommodating the volume change during the charge/discharge process, which are beneficial for achieving outstanding cyclic stability [27-31]. Moreover, redox-active polymers with high structural and thermal stability can be operated in a wide temperature range to extend the applications of RAOBs in extreme conditions and high/low-temperature regions. Currently, a few redox-active polymers based on carbonyl, imine, and amine groups have been investigated as the cathode materials in RAOBs due to their fast kinetics and high cyclic stability [27,31-33]. However, the reaction mechanism, interphase structure, and the impact of multi-functional groups in redox-active organic materials to the electrochemical performance of RAOBs remain elusive. Moreover, azo compounds, which have been employed as high-voltage catholyte materials in redox flow batteries, have never been investigated in RAOBs [34]. Hence, it is highly desirable to design advanced redox-active polymers with multi-active centers to exploit the structure-performance correlation, reaction mechanism, and interfacial chemistry in RAOBs.

Herein, we designed a redox-active polymer bearing both carbonyl and azo groups for RAOBs. The polymer was named as PNA and synthesized through a one-pot polycondensation reaction using naphthalenetetracarboxylic dianhydride (NTCDA) and 4,4'-azodianiline (ADA) as precursors (Fig. S1). Both the carbonyl and azo functional groups in PNA are the active sites that can reversibly react with Al complex carrier ions (AlCl₂⁺). The N-doped single layer graphene (NG) was employed as the conductive additive to replace carbon black (CB) and mixed with PNA when preparing the electrode (Fig. S2). The particle size of PNA was reduced after grinding and the mixing with NG,

which enhances the conductivity and shortens the ion/electron diffusion pathway. In addition, the voids between PNA and NG accommodate the volume change and maintain the structure integrity of the PNA/NG cathode during the repeated charge/discharge process (Fig. 1). Such a unique PNA/NG cathode exhibits a high reversible specific capacity (175 mAh g⁻¹ at the current density of 0.05 A g^{-1}), superior cyclability (10,000 cycles at the current density of 2 A g⁻¹), excellent rate capability (up to 10 A g^{-1}), and a wide operation temperature range (-40°C to 100 $^{\circ}$ C). The exceptional specific capacity is retained at high mass loading of 7 mg cm⁻², exhibiting a high areal capacity of 1.08 mAh cm⁻². To gain fundamental insight into the reaction mechanism and interfacial structure of the polymeric cathode, X-ray photoelectron spectroscopy (XPS), pair distribution function (PDF) analysis, and soft Xray absorption near edge structure (XANES) were employed, demonstrating the step-by-step redox reaction between carbonyl/azo groups in PNA and AlCl₂, as well as a stable Al₂O₃- and AlN-rich cathode electrolyte interphase (CEI) structure in RAOBs.

2. Results and Discussion

The molecular and crystalline structures of PNA were investigated by Fourier-transform infrared spectroscopy (FTIR), Raman spectroscopy, X-ray diffraction (XRD), and X-ray photoelectron spectroscopy (XPS). The intense absorption peaks at \sim 1715 and 1670 cm $^{-1}$ in the FTIR spectrum (Fig. 2a) represent the stretching vibrations of C=O groups. The absorption peaks at \sim 1590 cm $^{-1}$ in the FTIR spectrum confirm the existence of azo group, and the absorption peaks at \sim 1340 cm $^{-1}$ and 1240 cm $^{-1}$ in the FTIR spectrum are ascribed to the stretching vibrations

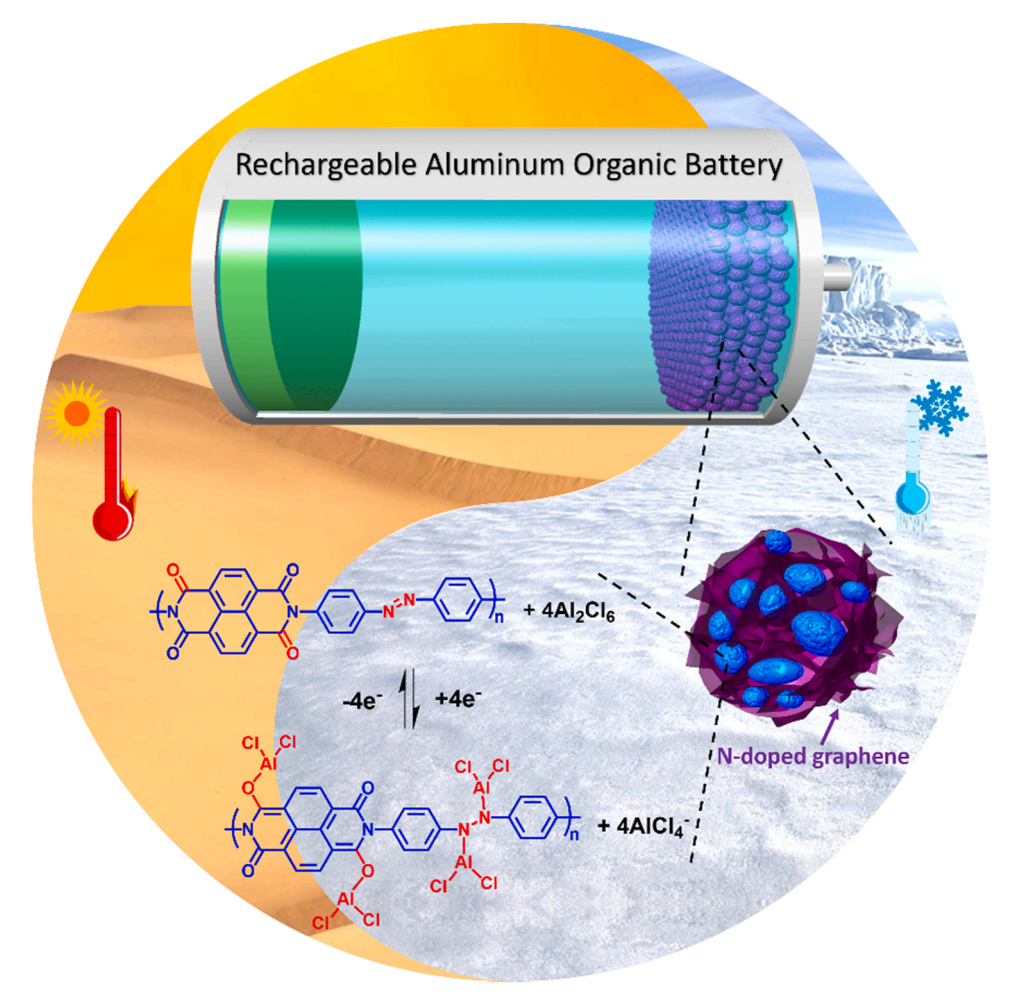


Fig. 1. Schematic illustration of the PNA-based RAOBs.

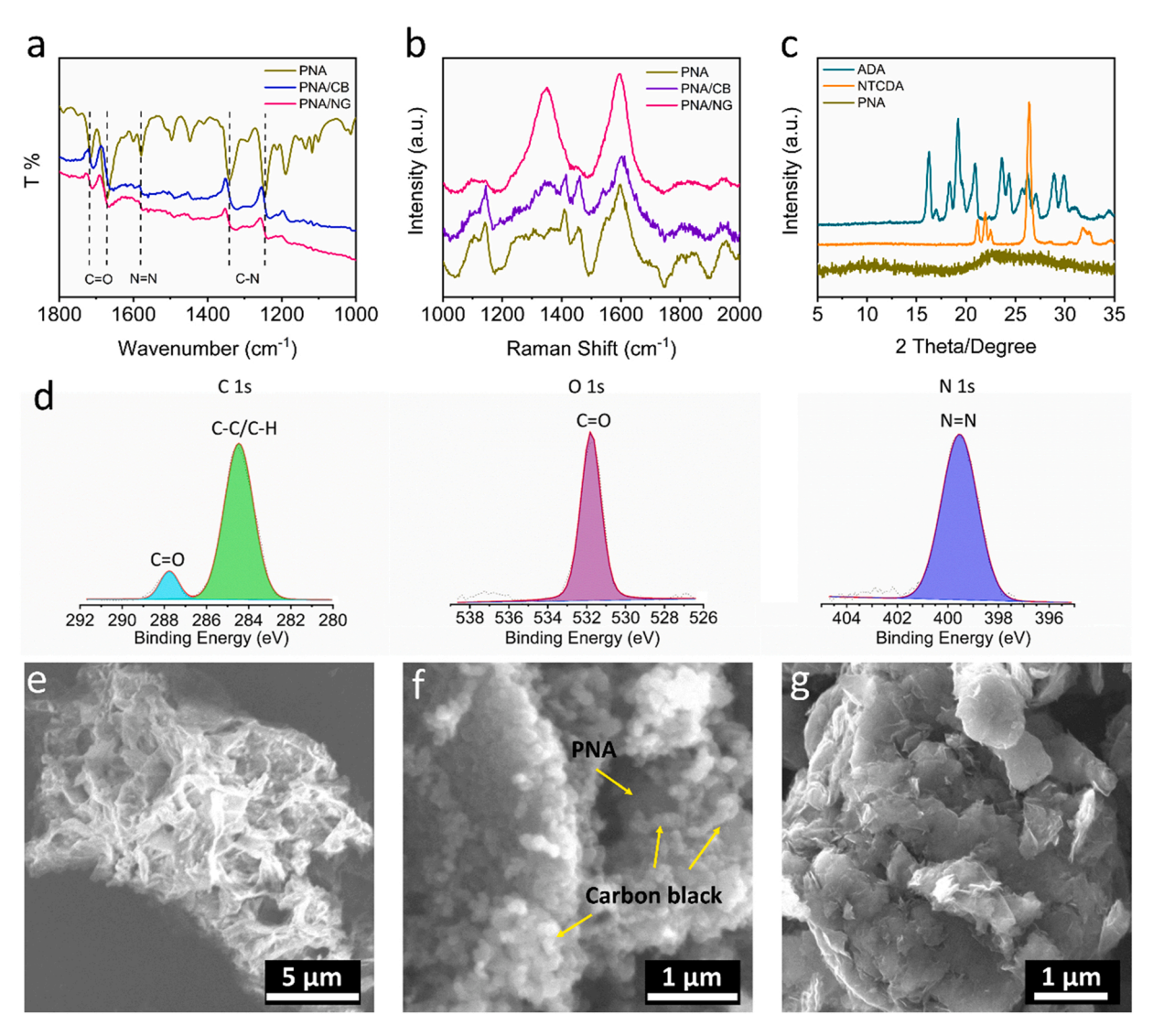


Fig. 2. Material characterizations. (a) The FTIR and (b) Raman spectra of PNA, PNA/CB and PNA/NG powders. (c) XRD spectrum of NTCDA, ADA and PNA powders. (d) High resolution XPS of C 1 s, O 1 s, and N 1 s spectra of PNA powder. The SEM images of (e) PNA, (f) PNA/CB and (g) PNA/NG powders.

of C-N groups [35]. All the peaks mentioned above have no obvious change after mixing with carbon black (CB) and NG, indicating the high structure stability of the prepared PNA. The Raman peaks at 1143, 1411 and 1457 cm⁻¹ represent the stretching vibration of the N=N group (Fig. 2b), while the peak located at 1598 cm⁻¹ demonstrates the existence of C=O groups [36]. Notably, most characteristic peaks of PNA are still observed after mixing with CB, but they are overlapped with D and G bands of NG. In the XRD patterns (Fig. 2c), unlike the crystalline NTCDA and ADA precursors, the obtained PNA is amorphous. The XPS spectra, which were calibrated by the C-C peak in C 1 s spectrum at 284.4 eV, exhibiting obvious peaks of C=O (287.7 eV in C1 s spectrum and 531.7 eV in O1s spectrum) and N=N (399.5 eV in N 1 s spectrum) (Fig. 2d) [36]. The single and strong peaks in O 1 s and N 1 s spectra prove the high purity of the obtained PNA. After mixing with NG, some functional groups from NG, such as C-O (oxygen residue), O-C=O (π - π conjugate) and Graphitic N (N-doping), are introduced in the PNA/NG composite (Fig. S3). The morphological structure of PNA was investigated by scanning electron microscopy (SEM), which demonstrates that the PNA powder exists as micro-sized particles with irregular shapes (Fig. 2e). The blurred image indicates the low conductivity of the raw PNA. In contrast, the PNA/CB and PNA/NG composites display enhanced conductivity with high-resolution SEM images (Fig. 2e and f). For the PNA/CB material, although carbon black nanoparticles are

uniformly distributed on the surface of PNA/CB composite, the PNA particles still can be observed (Fig. 2f). In contrast, the PNA particles with decreased size are fully coated with NG in the PNA/NG composite, and no raw PNA particles can be observed, demonstrating the uniform distribution of PNA in the composite (Fig. 2g and Fig. S4).

The electrochemical performance of the PNA/NG cathode in RAOBs was investigated by the Swagelok-type two-electrode cell system, which used the Al metal as the counter electrode and $AlCl_3$:EMImCl (1.5:1 in molar ratio) as the electrolyte. The electrochemical performance of PNA/NG cathode was tested in the cutoff window of 0.5-2.3 V. To confirm the cation that reacts with PNA, energy dispersive spectroscopy (EDS) was employed to investigate the discharged PNA/NG cathode at 0.5 V. The EDS mapping indicates that the elements of C, N, O, Al, and Cl are uniformly distributed on the surface of the PNA/NG cathode (Fig. S5). In addition, the EDS spectrum and elemental analysis demonstrate that the atomic ratio of Al and Cl is 0.75%:1.31%, which is close to 1:2, further proving the interaction between AlCl₂ and PNA in the cathode (Fig. S6 and Table S1). Fig. 3a shows the cyclic voltammetry (CV) curves of the PNA/NG cathode at the scan rate of 0.1 mV s⁻¹. Three cathodic peaks at 1.89/1.43/1.13 V and three anodic peaks at 1.28/ 1.55/2.05 V are observed. The two pairs of peaks located at 1.43/1.55 V and 1.13/1.28 V belong to the redox reaction between the carbonyl groups and AlCl₂ ions, and the pair of peaks located at 1.89/2.05 V

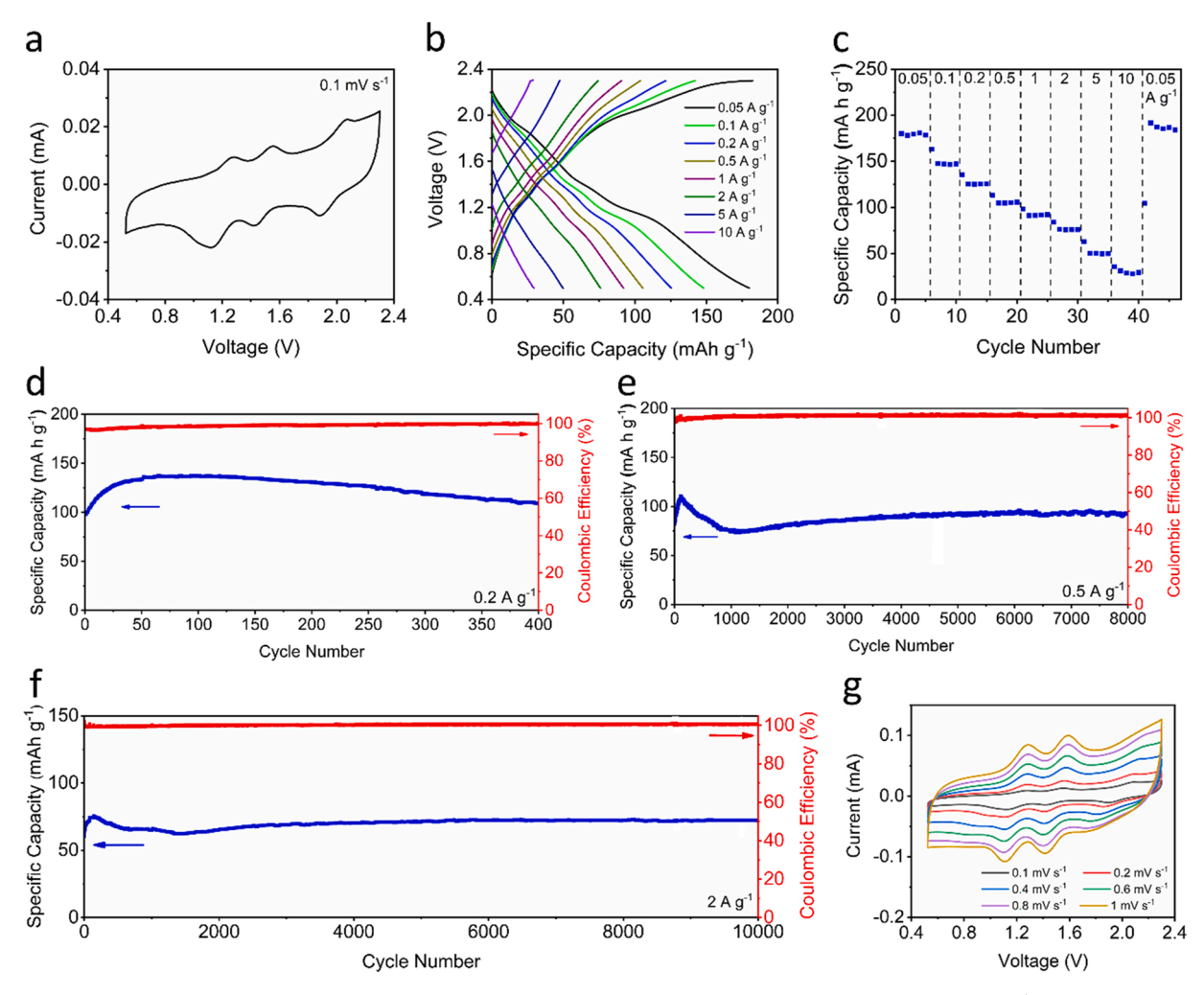


Fig. 3. Electrochemical performance of the PNA/NG cathode in RAOBs at room temperature. (a) Cyclic voltammograms at $0.1~\text{mV s}^{-1}$. (b) Charge/discharge curves of the PNA/NG cathode at different rates. (c) Rate performance of the PNA/NG cathode at various current densities. Discharge capacities and Coulombic efficiencies of the PNA/NG cathode measured at (d) 0.2, (e) 0.5, and (f) $2~\text{A g}^{-1}$. (g) Cyclic voltammograms at various scan rates.

relates with the reversible intercalation/de-intercalation of AlCl[†] in the azo group. Similarly, three cathodic peaks at 1.96/1.42/1.18 V and three anodic peaks at 1.22/1.51/2.06 V are observed in the PNA/CB cathode (Fig. S7a). In addition, there is no obvious CV peaks in the NG electrode in the cutoff window of 0.5-2.3 V (Fig. S7b) [37], which further proves that the pair of redox peaks higher than 1.6 V attributes to the reversible reaction between azo groups and AlCl₂ ions. Fig. S8 shows the charge/discharge curves of the PNA/NG cathode at the current densities of 20 and 50 mA g⁻¹, respectively. The PNA/G cathode delivers a discharge capacity of 225.1 mAh g⁻¹ at the current density of 20 mA g⁻¹, which is comparable with the theoretical capacity of PNA material. In contrast, an obvious capacity decrease was observed after elevating the current density to 50 mA g⁻¹ (178.2 mAh g⁻¹) due to the high viscosity and slow ion transport kinetics of the ionic liquid electrolyte. Moreover, the electrolyte decomposition at the high voltage range becomes worse along with the decrease of current densities, leading to the abnormal Coulombic efficiency (>100%) of the PNA/NG cathode at the current density of 20 mA g⁻¹. To mitigate electrolyte decomposition and maintain a reasonable Coulombic efficiency, the electrochemical performance of cathode materials was investigated at the current densities of 50 mA g⁻¹ or above. To further understand the role of NG in the performance of the polymeric cathode, the comparison of the charge/discharge curves of PNA/NG, PNA/CB, NG and CB electrodes at the current density of 0.05 A g⁻¹ was provided (Fig. S9). NG and CB do not show obvious reversible redox plateaus, and they deliver

specific capacities of 20.9 and 7.3 mAh $\rm g^{-1}$ in the cutoff window of 0.5–2.3 V, respectively, which don't have a crucial contribution to the capacity of the cathode. The PNA/NG cathode exhibits similar charge/discharge curves with that of the PNA/CB cathode but delivers a much higher specific capacity (178.2 mAh $\rm g^{-1}$ versus 124.5 mAh $\rm g^{-1}$ for the PNA/CB cathode). The NG coating can effectively enhance the electrode conductivity and facilitate the reversible interaction of aluminum complex ions with the cathode material, resulting in an improved electrochemical performance in RAOBs.

To further assess the performance in RAOBs, rate capability and long-term cyclic stability tests were carried out. The PNA/NG cathode displays excellent rate capability at room temperature, delivering the specific capacity of 178.2, 147.9, 126.3, 106.3, 92.6, 76.9, 51.1 and 31.5 mAh g^{-1} at the current densities of 0.05, 0.1, 0.2, 0.5, 1, 2, 5 and 10 A g^{-1} . The specific capacity recovers to 185.1 mAh g^{-1} immediately after the current density reduces back to 0.05 A g^{-1} , indicating the robust reaction kinetics. Notably, the comparison of the charge/discharge curves at the current densities of 20 and 50 mA g^{-1} indicates that the capacity of the discharge plateau at $\sim\!1.9$ V shows obvious decrease, but the capacity of the discharge plateaus at $\sim\!1.4/1.2$ V almost have no change when the current density increases from 20 mA g^{-1} to 50 mA g^{-1} , suggesting that the N=N group doesn't show as good rate capability as the C=O group (Fig. S8). In addition to the superior rate capability, the PNA/NG cathode also exhibits outstanding cyclic stability at room temperature. At the low current density of

0.2 A g⁻¹, the PNA/NG cathode delivers an initial reversible capacity of 98.5 mAh g⁻¹ and increases to 136.7 mAh g⁻¹ after a few cycles due to the activation process caused by the high-viscosity electrolyte infiltration. Afterwards, the reversible specific capacity gradually decreases due to the irreversible decomposition of the electrolyte at the high voltage and the inevitable dissolution of the fully discharged organic cathode material. However, a high capacity of 112.3 mAh g⁻¹ can still be retained after 400 cycles (Fig. 3d) [33]. Meanwhile, the PNA/NG cathode displays excellent cyclic stability at high current densities. At 0.5 A g⁻¹, the PNA/NG cathode delivers an initial specific capacity of 82.5 mAh g $^{-1}$ and remains 92.1 mAh g $^{-1}$ after 8000 cycles (Fig. 3e). At 2 A g $^{-1}$, it provides a maximum reversible capacity of 74.7 mAh g $^{-1}$ and retains at 72.5 mAh g⁻¹ after 10,000 cycles with an excellent capacity retention of 97% (Fig. 3f). The exceptional performance is retained at a high mass loading of 7 mg cm⁻², which delivers a specific capacity of 151.2 mAh g⁻¹ and an areal capacity of 1.08 mAh cm⁻² at 50 mA g⁻¹ (Fig. S10). To investigate the reaction kinetics of the PNA/NG cathode in RAOBs, cyclic voltammetry under different scan rates from 0.1 to 1 mV s⁻¹ was performed. As shown in Fig. 3g, the cathodic peaks shift to a lower voltage region, and the anodic peaks shift to a higher voltage region with the elevated scan rates because of the increased polarization [38]. The TEM image of PNA/NG indicates that the size of PNA particles was reduced to nanoscale, and PNA is fully coated with NG after ball milling, which can effectively increase the specific surface area of PNA particles (Fig. S4). The increased surface area of PNA and the coating of NG with high electrical conductivity synergistically promote the surface redox reaction of the PNA cathode. As expected, the slope (b) values of anodic and cathodic peaks corresponding to the pair of peaks located at 1.43/1.55 V are 0.7656 and 0.7768, respectively, further proving the hybrid reaction mechanism of diffusion and pseudocapacitive behaviors (Fig. S11) [39]. The pseudocapacitive reaction mechanism contributes to the fast kinetics of the PNA/NG cathode. Therefore, the PNA/NG composite is a promising organic cathode material for high-capacity, high-rate, and ultra-stable RAOBs.

To expand practical applications of RAOBs in tropical zone, north/ south poles, and other extreme conditions, the electrochemical performance at high and low temperatures is crucial. Hence, the electrochemical performance of the PNA/NG cathode in the temperature range from - 40°C to 100 °C is assessed. To mitigate electrolyte decomposition and maintain the high Coulombic efficiency, the cutoff voltage was optimized at different temperatures [37]. Fig. 4a shows the galvanostatic charge/discharge curves of the PNA/NG cathode in the temperature range from 25 °C to 100 °C under the current density of 0.2 A g^{-1} . A higher specific capacity of 143.5 mAh g⁻¹ is achieved at 60 °C compare with that at 25 °C due to the enhanced ion diffusion rate at high temperature. The PNA/NG cathode delivers a maximum capacity of 154.1 mAh g⁻¹ at 80 °C and gradually decreases to 115.2 mAh g⁻¹ at 100 °C due to the reduced cutoff window. As shown in Fig. 4b, the PNA/NG cathode exhibits superior stability in the wide temperature ranges from 25 to 100 °C with high Coulombic efficiency. Excellent cyclic stability of 85.6% capacity retention can be retained after 300 cycles at 80 °C (Fig. 4c), demonstrating stable electrochemical performance at high temperatures.

Additionally, the PNA/NG cathode also affords remarkable electrochemical performance at low temperatures. The PNA/NG-based RAOBs was operated at low temperatures from 0 to -40°C . As shown in Fig. 4d and e, the PNA/NG cathode delivers stable specific capacity of 138.7 mAh g $^{-1}$ at the current density of 0.02 A g $^{-1}$ and 0 °C. A specific capacity of 125.5 mAh g $^{-1}$ is retained at -20°C , and negligible capacity decay is observed even though the operation temperature decreases to -30°C (124.8 mAh g $^{-1}$). More importantly, the PNA/NG cathode still retains a specific capacity of 105.4 mAh g $^{-1}$ at a current density of 0.05 A g $^{-1}$ with 88% capacity retention after 300 cycles (Fig. 4 f). Large overpotential and voltage drop are observed at the operation temperature of -40°C due to the high viscosity of the ionic liquid electrolyte and sharply reduced ion diffusion rate at such a low temperature (Fig. S12a). A specific capacity of 70.2 mAh g $^{-1}$ is achieved and retained at the current density of 0.01 A g $^{-1}$ and -40°C (Fig. S12b). Therefore,

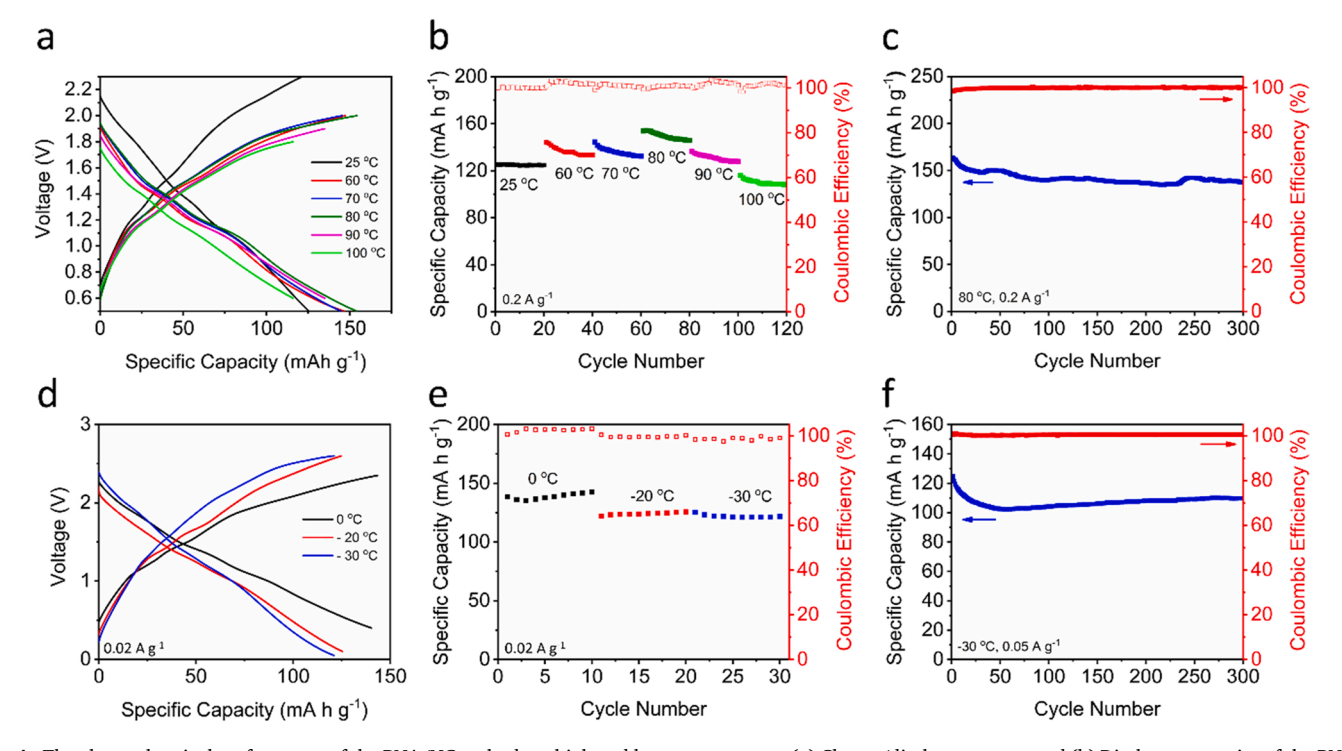


Fig. 4. The electrochemical performance of the PNA/NG cathode at high and low temperatures. (a) Charge/discharge curves and (b) Discharge capacity of the PNA/NG cathode at different high temperatures under the current density of 0.2 A g^{-1} . (c) Cycling performance of the PNA/NG cathode at 80 °C under the current density of 0.2 A g^{-1} . (d) Charge/discharge curves and (e) Discharge capacity of the PNA/NG cathode at different low temperatures under the current density of 0.02 A g^{-1} . (f) Cycling performance of PNA/NG cathode measured at -30 °C under the current density of 0.05 A g^{-1} .

the PNA/NG cathode exhibits excellent electrochemical performance at both high and low temperatures, attributing to the unique structure of the polymer cathode and superior thermal stability of the ionic liquid electrolyte.

To gain fundamental insight into the impressive electrochemical performance of the PNA/NG cathode, XPS, PDF, and soft XANES are used to study the CEI structure, reaction mechanism, as well as structural evolution of the cycled electrodes. The CEI chemical composition was investigated by XPS with an Ar+ sputtering depth profiling after cycling (Fig. 5). The O 1 s XPS spectrum at 531.1 eV for Al-O, the N 1 s XPS spectrum at 398.3 eV for Al-N, and the Al 2p XPS spectrum at 73.8 and 74.8 eV for Al-O and Al-N are observed on the top surface of the PNA/NG cathode after cycling, indicating that $\mathrm{Al}_2\mathrm{O}_3$ and AlN are the key components in the CEI [40–45]. After sputtering for 300 s, the intensity of XPS peaks for Al-O and Al-N has no obvious change but dramatically decreases after sputtering for 600 s and 900 s, while no new peak appears, which further confirms that the key components in the CEI are Al₂O₃ and AlN. A stable and robust Al₂O₃- and AlN-rich CEI is critical for the high stability of the RAOBs. The area ratio of Al-Cl 2p1/2 and Al-Cl 2p3/2 of Cl 2p XPS spectra changes along with the extension of sputtering time due to the gradual reduction of the residual electrolyte on the surface of the cathode material. Besides, Ar⁺ has a certain reducibility. It will cause reduction of some elements, and broadened peaks can be observed at low binding energy positions.

The reaction mechanism and structural evolution of the PNA/NG cathodes were also exploited at different discharged/charged states marked in Fig. 6a. The C 1 s, O 1 s and N1s XPS spectra of the pristine PNA/NG cathode show no obvious difference with that of the PNA/NG powder (Fig. 6b). After discharging to 1.6 V, the intensity of O 1 s XPS peaks of C=O group has no obvious change, but the intensity of the N 1 s XPS peak of the Al-N group is increased, while the N 1 s XPS peak of the N=N group is decreased, indicating that the discharge plateau above

1.6 V is due to the reaction between AlCl₂ cations and N=N groups (Fig. 6c). After further discharging to 1.3 V, the intensity of O 1 s XPS peaks of the C=O group reduces and O 1 s XPS peaks of the C-O group raises, because of the reaction between the AlCl₂⁺ cations and the carbonyl groups (Fig. 6d). After discharging to 0.5 V, the intensity ratio of peaks related with C-O and C=O groups further increases, indicating the continued reaction between carbonyl groups and AlCl₂ cations. Meanwhile, the intensity of the N 1 s XPS peak of Al-N group gradually increases, and the N 1 s XPS peak of N=N group gradually decreases along with the continuous discharging, demonstrating further reaction between AlCl₂⁺ cations and the N=N groups under 1.6 V (Fig. 6e). During the charging process (Fig. 6f-h), the intensity ratio of the C-O peak to the C=O peak gradually decreases with the increase of the voltage, while the intensity of the N 1 s XPS peak for Al-N obviously decreases, and the intensity of the N 1 s XPS peak for N=N obviously increases, verifying the reversible reaction between N=N/C=O groups and AlCl2 cations.

To further prove that the N=N groups react with AlCl₂⁺ cations in the cutoff voltage range of 0.5–2.3 V, two more NTCDA-based polymers, DAC-PI and EDA-PI, were synthesized (Fig. S13). Fig. S14 shows the charge/discharge curves of DAC-PI/NG, EDA-PI/NG and PNA/NG cathodes at the current density of 0.05 A g⁻¹. The absence of the redox plateaus at high voltage above 1.8 V for both DAC-PI/NG and EDA-PI/NG cathodes materials without N=N groups further demonstrates the interaction between N=N groups and AlCl₂⁺ cations at a relatively high voltage in the PNA/NG cathode. In addition, the DAC-PI/NG cathode exhibits much better cyclic stability than that of the EDA-PI/NG cathode, demonstrating that the benzene ring in DAC-PI can effectively enhance the structure stability of the DAC-PI/NG cathode during the repeated charge/discharge process due to the conjugation effect with NG (Fig. S15). There are two benzene rings at each end of the azo group in PNA, hence, this will enhance the cyclic stability of the PNA/NG

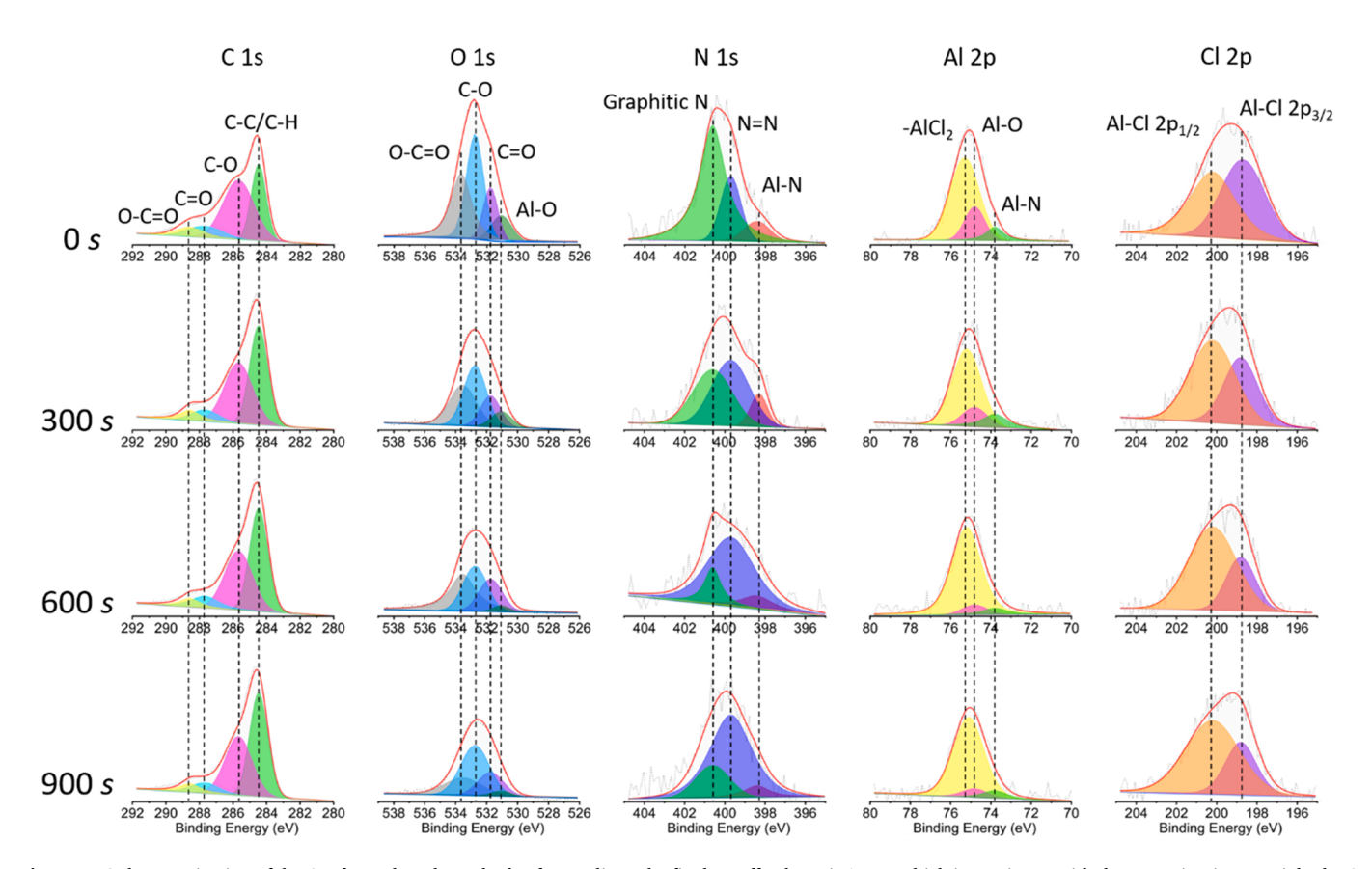


Fig. 5. XPS characterization of the CEI formed on the cathode after cycling. The final cutoff voltage is 1.7 V, which is consistent with the open circuit potential. The C 1 s, O 1 s, N 1 s, Al 2p and Cl 2p spectra are displayed in columns, which show the corresponding depth profiling results.

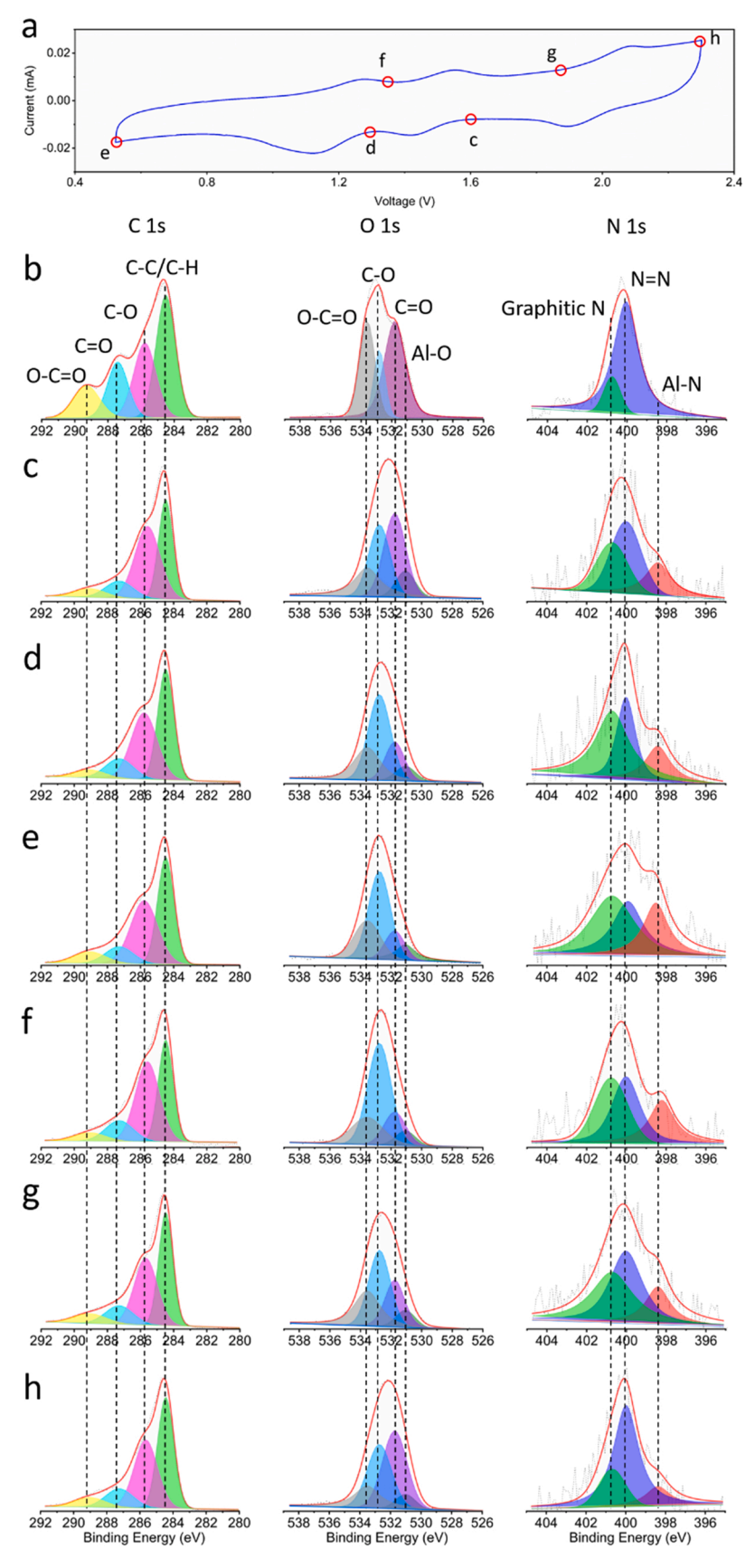


Fig. 6. XPS characterization of the pristine and cycled PNA/NG cathodes at different states of discharge and charge. (a) CV profiles of the PNA/NG cathode at the scan rate of 0.1 mV s⁻¹; (b) C 1 s, O 1 s and N 1 s XPS spectra of the pristine PNA/NG cathode, and the PNA/NG cathode at states of (c) discharged to 1.6 V, (d) discharged to 1.3 V, (e) discharged to 0.5 V, (f) charged to 1.35 V, (g) charged to 1.9 V and (h) charged to 2.3 V. The discharged/charged points at which the measurements were carried out are indicated in (a).

cathode.

To further confirm the reaction mechanism, PDF and soft XANES measurements were also conducted. As a total scattering technique, PDF serves as an ideal tool for probing bulk structure evolution for organic materials during electrochemical cycling [46,47]. PDF results of the PNA polymer, NG and PNA/NG cathode are shown in Fig. 7a. Peaks 1, 2 and 3 mainly correspond to various C-C correlations inside aromatic rings which are present in all samples (Fig. 7b). Peak 1 for the PNA polymer and PNA/NG cathode has obvious contributions from the low r part which is attributed to the short C=O (1.23 Å) and N=N (1.22 Å) correlations in the polymer. The small peaks at around 1.8 Å and 2.1 Å are so-called 'termination ripples' that come from the finite range of the Q-space data being Fourier transformed [48]. Fig. 7c shows the ex-situ PDF results of PNA/NG cathodes, revealing how those bonds of interest evolve during electrochemical cycling. Note that the amplitude of 'termination ripples' does not change for different data in Fig. 7c because the same Q range is always used for Fourier transform. However, the amplitude of 1.8 Å and 2.1 Å peaks are obviously different for those ex-situ samples. This suggests that during the charge-discharge process, chemical bonds of relevant bond lengths are involved. The 1.8 Å and 2.1 Å peaks should correspond to Al-O/N and Al-Cl bonds respectively because peak positions match very well with the bond lengths. They gradually grow during discharge and reach the maximum when the electrode is fully discharged (discharged to 0.5 V), followed by a decrease during the charge process. These suggest Al is added to the PNA/NG structure during discharge and released during charge. To

understand the evolution of electrochemically relevant bonds such as C=O/N=N and C-O/N-N, the first PDF peak is deconvoluted by using three Gaussian peaks, corresponding to C=O/N=N, C-C, and C-O/N-N, respectively (Fig. 7d). The intensity of the C=O/N=N peak decreased during discharge and increased during charge, indicating the destruction (discharge) and formation (charge) of these bonds upon addition and removal of the AlCl₂ cations. On the other hand, the intensity of the C-O/N-N peak increased during discharge and decreased during charge, suggesting the formation (discharge) and destruction (charge) of those bonds during cycling. After one full cycle, the intensity of both C=O/N=N and C-O/N-N peaks are fully restored to those in the pristine state, suggesting the reversible structural change during electrochemical cycling.

Understanding of the reaction mechanism is further complemented by soft X-ray spectroscopy studies at both O and N K-edges. Partial fluorescence yield (PFY) mode detection enables relatively bulk probe (~ 100 nm). The PFY mode of O K-edge XANES spectra consist of peaks arising from both the NG (indicated by the 531 eV peak corresponding to C-O=C) and the PNA polymer (indicated by the 532.5 eV peak corresponding to the N-O=C). The N-O=C peak decreases during discharge and increases during charge, suggesting the cleavage and reformation of C=O bonds (Fig. 8a). Similar behavior is observed for the N=N peak in the PFY mode of N K-edge XANES spectra (Fig. 8b), confirming the redox reaction of the N=N bond with AlCl½. These are consistent with previous XPS and PDF results, confirming our proposed reaction mechanism. In addition, the Raman spectra of the PNA/CB cathode at different

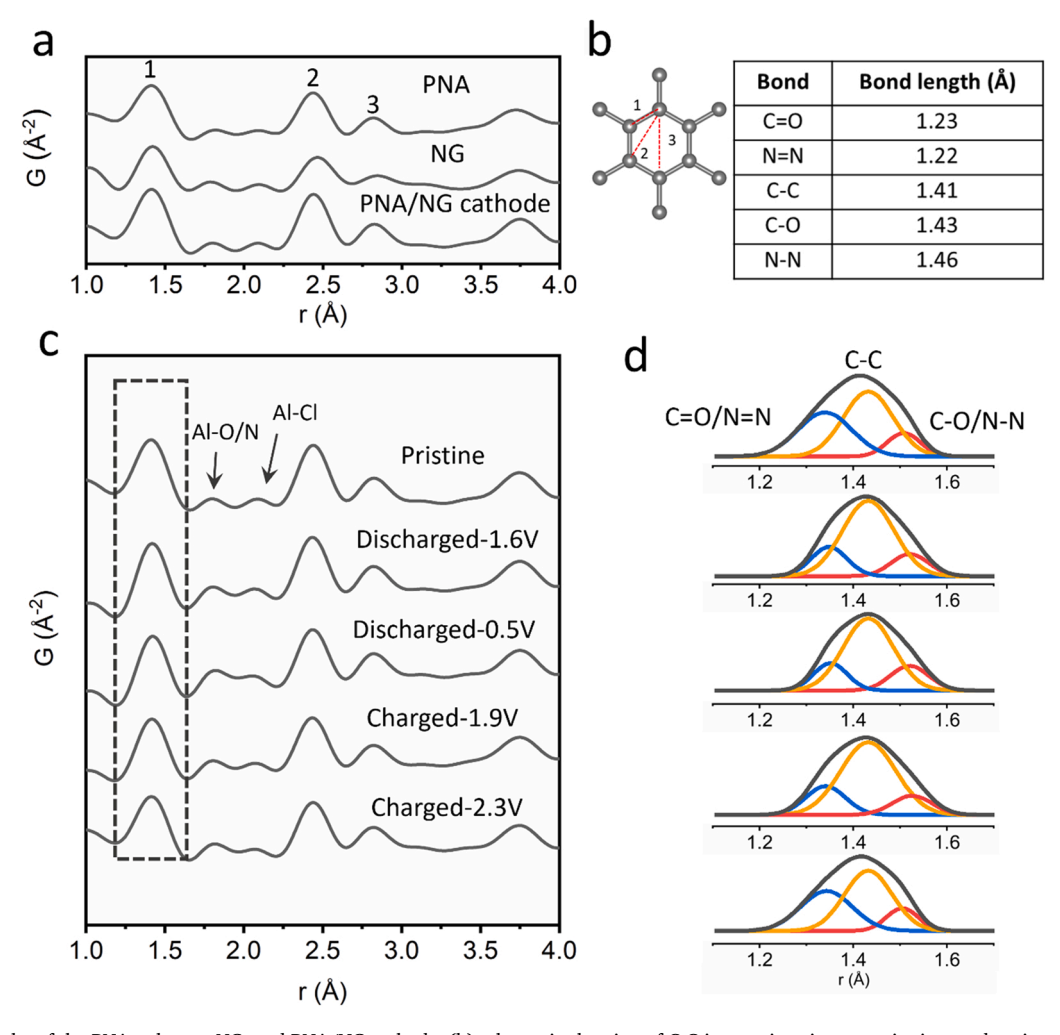


Fig. 7. (a) PDF results of the PNA polymer, NG, and PNA/NG cathode. (b) schematic showing of C-C interactions in aromatic ring, and various bond lengths in the structure. (c) Ex-situ PDF results of the cycled PNA/NG cathodes. (d) Deconvolution of the PDF peaks in the dash area of (c).

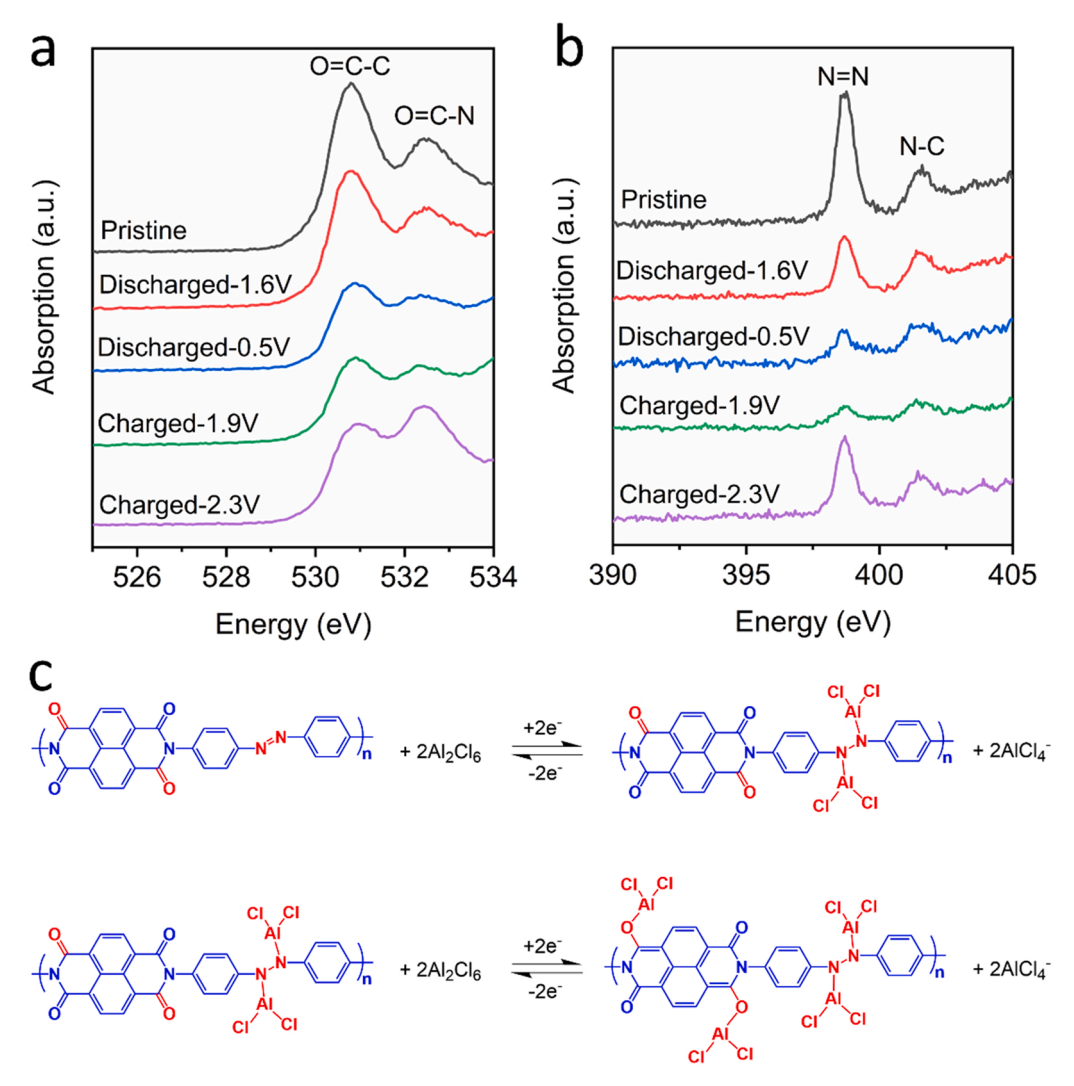


Fig. 8. Soft XANES results of ex situ electrodes at (a) O K-edge and (b) N K-edge in PFY mode. (c) The electrochemical reaction mechanism of the PNA cathode.

discharge/charge states were investigated to further prove the reaction mechanism of PNA. As shown in Fig. S16, the intensities of N=N peaks located at 1143, 1411 and 1457 cm⁻¹ almost disappear after discharging to 1.6 V and reappear after charging to above 1.9 V, demonstrating the interaction of the N=N group with AlCl₂ at the high voltage. Although the peak for the C=O group overlaps with the G band of carbon black at ~1590 cm⁻¹, the reaction mechanism of C=O group still can be investigated through the changes of the intensity ratio of D band (\sim 1360 cm⁻¹) and C=O/G band (\sim 1590 cm⁻¹). Compared with the pristine PNA/CB cathode, the intensity ratio of D band and C=O/G band is constant after discharging to 1.6 V and gradually increases along with the further discharge. During the charge process, the intensity ratio of D band and C=O/G band decreases and recovers to the initial stage after charging to 1.9 V, indicating the cleavage and reformation of C=O at the relatively low voltage. According to the above mechanical study, the redox mechanism of the PNA cathode in RAOBs is illustrated in Fig. 8c, the two carbonyl groups in the repeating unit of PNA react with $AlCl_2^+$ step-by-step at ~1.5 V and ~1.2 V, accompanied by intramolecular electron transfer in the NTCDA moieties, and then the azo groups react with $AlCl_2^+$ at \sim 2 V. The highly reversible redox reactions between carbonyl/azo groups and AlCl2+, as well as the stabilization by NG, enable the impressive performance of the RAOBs.

3. Conclusion

In conclusion, PNA with bifunctional active centers (carbonyl and azo groups) was prepared and employed as an organic cathode for RAOBs. The bifunctional groups endow PNA a high reversible capacity through the reversible reaction with Al complex carrier ions (AlCl₂), moreover, the introducing of NG effectively increases the conductivity of PNA and accommodates the large volume change during the repeated charge/discharge process, improving the electrochemical performance of RAOBs. The PNA/NG cathode delivers excellent electrochemical performance, in terms of high specific capacity, fast-charging capability, long cycling stability, and a wide operation temperature range. The interfacial chemistry and reaction mechanism of the PNA/NG cathode were studied by XPS, PDF, and soft XANES, confirming the Al₂O₃ and AlN as the key components in the CEI layer, as well as the step-by-step redox reaction mechanism between carbonyl/azo groups and AlCl₂. Thus, our finding opens up a new opportunity for the design of fastcharging and sustainable all-climate rechargeable aluminum batteries.

Experimental section/methods

Materials: Naphthalenetetracarboxylic dianhydride (NTCDA) (>97%), 4,4'-Azodianiline (ADA) (95%), trans-1,4-diaminocyclohexane (DAC) and ethylenediamine (EDA) were purchased from TCI, and they were used as received. Dimethylformamide (99.8%) was purchased from

Sigma-Aldrich and stirred for 24 h with Magnesium Sulfate to remove any trace of water before using it for synthesis. The N-doped single layer Graphene was received from ACS materials, and carbon black (Super P) with above 99% purity was purchased from Alfa Aesar. 1-Ethyl-3-methylimidazolium chloride (EMImCl) (99%) and $AlCl_3$ (99.95%) were purchased form Sigma-Aldrich.

Synthesis of PNI, DAC-PNA and EDA-PNA: For the synthesis of PNA, naphthalenetetracarboxylic dianhydride (NTCDA) was dissolved in 30 mL of Dimethylformamide (DMF) in a 100 mL three-necked flask under refluxing and degassing. 4,4′-Azodianiline was dissolved in 10 mL of DMF and added to the solution stirring at 140 °C under Nitrogen gas and continued under $\rm N_2$ atmosphere for 3 days. The obtained amber color precipitation was collected by centrifuge and washed with methanol and acetone 3 times, respectively. The resulting solid was dried at 80 °C in a vacuum oven. The processes for the synthesis of DAC-PNA and EDA-PNA are similar with that of PNA, which used DAC or EDA replace the ADA precursor.

Characterizations: X-ray diffraction (XRD) pattern was recorded by Rigaku MiniFlex using CuKα radiation; Fourier transform infrared spectroscopy (FTIR) was recorded by Agilent Cary 630 FTIR Spectrometer; The morphologies of electrode materials were observed by SEM (JEOL JSM-IT500HR); Raman spectroscopy was recorded by Horiba XploRA PLUS Raman microscope with a 532 nm laser. XPS measurements were carried out at a PHI 5000 VersaProbe II system (Physical Electronics) spectrometer, which is equipped with a hemispherical analyzer. The spectrometer is attached to the Ar glovebox and sample transfer was directly through it to avoid any contact of the samples with air and moisture. Monochromatic Al-K α excitation (h ν = 1486.6 eV) was used at power of 25 W, additionally applying a low-energy electron charge neutralizer. The high-resolution spectrum of each element was collected with a pass energy of 23.25 eV in an analysis area of 100 * 100 μm. The binding energy scale was corrected based on the C1s peak from contaminations (C-C at 284.4 eV) as internal binding energy standard. Pair distribution function (PDF) characterization of the organic electrodes was carried out at beamline 28-ID-2 of the National Synchrotron Light Source II (NSLSII) at BNL, using a photon wavelength of 0.18475 Å. PDF data were collected using an amorphous silicon flat panel two-dimensional detector (Perkin Elmer) and radially integrated using Fit2D software [49]. The exposure time of ex situ measurements was typically around 1 h for each sample. The PDF and G(r) values were extracted using PDFgetX3 software [50]. The soft XAS measurements at C, N and O K-edge were performed in partial fluorescence yield (PFY) at IOS beamline in NSLS II. The collected soft XAS data were analyzed using the ATHENA software package [51].

Electrochemical measurements: The PNA polymer was grinded with NG or CB with the mass ratio of 5-4 for about one hour to make a homogenous mixture. 10 wt% of sodium alginate binder was added subsequently to form a slurry. The electrodes were prepared by casting the slurry onto Mo foil using a doctor blade and dried in a vacuum oven at 80 °C overnight to prepare the PNA/NG or PNA/CB cathode. The slurry coated on Mo foil was punched into circular electrodes with a mass loading of \sim 1 mg cm⁻². For the preparation of electrodes with high mass loading (7 mg cm⁻², based on the mass of PNA), the grinded PNA/ NG powder was mixed with polytetrafluoroethylene (PTFE) binder at the weight ratio of 90:10, a thick film was obtained directly after grinding for 20 min. The thick film was cut into small pieces, and each piece was pressed together with a Mo mesh. The electrode with high mass loading was obtained after drying in a vacuum oven at 80 °C overnight. The RAOBs electrolyte was prepared inside a glovebox. AlCl₃ was slowly added to EMImCl in a molar ratio of 1.5:1, and then the mixture was stirred for a further 2 h to form an electrolyte with lightyellowish color. After that, 8 pieces of Al foil were emerged in the obtained electrolyte and stirred for a further 48 h. Swagelok-type batteries were assembled to investigate the electrochemical performance of different cathodes, which use Al metal as the counter electrode, and glass fiber (Whatman) as the separator. The entire batteries assembly

process was operated inside an argon-filled glovebox. Electrochemical performance was tested using Landt or Arbin battery test system. Cyclic voltammograms were recorded using Gamry Reference 1010E Potentiostat/Galvanostat/ZRA with a scan rate of 0.1–1 mV s $^{-1}$. Impedance analysis was also performed by Gamry Reference 1010E Potentiostat/ Galvanostat/ZRA.

CRediT authorship contribution statement

Kaiqiang Qin: Methodology, Validation, Investigation, Data Curation, Writing – original draft. Sha Tan: Methodology, Validation, Investigation, Data curation, Writing – review & editing. Motahareh Mohammadiroudbari: Methodology, Investigation, Data curation. Zhenzhen Yang: Methodology, Validation, Investigation. Xiao-Qing Yang: Supervision, Funding acquisition. Enyuan Hu: Methodology, Writing – review & editing, Supervision, Funding acquisition. Chao Luo: Conceptualization, Methodology, Writing – review & editing, Supervision, Project administration, Funding acquisition.

Declaration of Competing Interest

The authors declare that they have no known competing financial interests or personal relationships that could have appeared to influence the work reported in this paper.

Data Availability

Data will be made available on request.

Acknowledgements

This work was supported by the US National Science Foundation Award No. 2000102 and the George Mason University, College of Science Postdoctoral Fellowship. The authors also acknowledge the support from the George Mason University Quantum Science & Engineering Center. We gratefully acknowledge support from the Post Test Facility at Argonne National Laboratory, which is operated for DOE Office of Science by UChicago Argonne, LLC, under contract number DE-AC02–06CH11357. S. Tan, X.-Q. Yang, and E. Hu are supported by the Assistant Secretary for Energy Efficiency and Renewable Energy, Vehicle Technology Office of the U.S. Department of Energy through the Advanced Battery Materials Research (BMR) Program under Contract DE-SC0012704. This research used beamline 23-ID-2 and 28-ID-2 of the National Synchrotron Light Source II, a US DOE Office of Science user facility operated for the DOE Office of Science by Brookhaven National Laboratory under contract no. DE-SC0012704.

Appendix A. Supporting information

Supplementary data associated with this article can be found in the online version at doi:10.1016/j.nanoen.2022.107554.

References

- [1] X. Zhang, L. Li, E. Fan, Q. Xue, Y. Bian, F. Wu, R. Chen, Toward sustainable and systematic recycling of spent rechargeable batteries, Chem. Soc. Rev. 47 (2018) 7239–7302.
- [2] E. Fan, L. Li, Z. Wang, J. Lin, Y. Huang, Y. Yao, R. Chen, F. Wu, Sustainable recycling technology for li-ion batteries and beyond: challenges and future prospects, Chem. Rev. 120 (2020) 7020–7063.
- [3] D. Larcher, J.M. Tarascon, Towards greener and more sustainable batteries for electrical energy storage, Nat. Chem. 7 (2015) 19–29.
- [4] M.M. Titirici, Sustainable Batteries—Quo Vadis? Adv. Energy Mater. 11 (2021), 2003700.
- [5] C.P. Grey, J.M. Tarascon, Sustainability and in situ monitoring in battery development, Nat. Mater. 16 (2016) 45–56.
- [6] J. Piątek, S. Afyon, T.M. Budnyak, S. Budnyk, M.H. Sipponen, A. Slabon, Sustainable Li-Ion batteries: chemistry and recycling, Adv. Energy Mater. (2020), 2003456.

- [7] H. Yaghoobnejad Asl, A. Manthiram, Toward sustainable batteries, Nat. Sustain. 4 (2021) 379–380.
- [8] Y. Lu, Q. Zhang, L. Li, Z. Niu, J. Chen, Design strategies toward enhancing the performance of organic electrode materials in metal-ion batteries, Chem 4 (2018) 2786–2813.
- [9] K. Qin, J. Huang, K. Holguin, C. Luo, Recent advances in developing organic electrode materials for multivalent rechargeable batteries, Energy Environ. Sci. 13 (2020) 3950–3992.
- [10] J. Xie, Q. Zhang, Recent progress in multivalent metal (Mg, Zn, Ca, and Al) and metal-ion rechargeable batteries with organic materials as promising electrodes, Small 15 (2019), 1805061.
- [11] S. Chen, D. Zhao, L. Chen, G. Liu, Y. Ding, Y. Cao, Z. Chen, Emerging intercalation cathode materials for multivalent metal-ion batteries: status and challenges, Small Struct. 2 (2021), 2100082.
- [12] D. Ye, B. Luo, G. Lu, L. Wang, Will new aluminum-ion battery be a game changer? Sci. Bull. 60 (2015) 1042–1044.
- [13] Q. Liu, H. Wang, C. Jiang, Y. Tang, Multi-ion strategies towards emerging rechargeable batteries with high performance, Energy Storage Mater. 23 (2019) 566–586
- [14] A. Ponrouch, J. Bitenc, R. Dominko, N. Lindahl, P. Johansson, M.R. Palacin, Multivalent rechargeable batteries, Energy Storage Mater. 20 (2019) 253–262.
- [15] F. Wu, H. Yang, Y. Bai, C. Wu, Paving the path toward reliable cathode materials for aluminum-ion batteries, Adv. Mater. 31 (2019), 1806510.
- [16] S. Wang, S. Huang, M. Yao, Y. Zhang, Z. Niu, Engineering active sites of polyaniline for AlCl² storage in an aluminum-ion battery, Angew. Chem. 132 (2020) 11898–11905
- [17] M.C. Lin, M. Gong, B. Lu, Y. Wu, D.Y. Wang, M. Guan, M. Angell, C. Chen, J. Yang, B.J. Hwang, H. Dai, An ultrafast rechargeable aluminium-ion battery, Nature 520 (2015) 325–328.
- [18] D.Y. Wang, C.Y. Wei, M.C. Lin, C.J. Pan, H.L. Chou, H.A. Chen, M. Gong, Y. Wu, C. Yuan, M. Angell, Y.J. Hsieh, Y.H. Chen, C.Y. Wen, C.W. Chen, B.J. Hwang, C. C. Chen, H. Dai, Advanced rechargeable aluminium ion battery with a high-quality natural graphite cathode, Nat. Commun. 8 (2017) 14283.
- [19] X. Yu, B. Wang, D. Gong, Z. Xu, B. Lu, Graphene nanoribbons on highly porous 3d graphene for high-capacity and ultrastable Al-Ion batteries, Adv. Mater. 29 (2017), 1604118
- [20] Y. Zhang, S. Liu, Y. Ji, J. Ma, H. Yu, Emerging nonaqueous aluminum-ion batteries: challenges, status, and perspectives, Adv. Mater. 30 (2018), 1706310.
- [21] T. Koketsu, J. Ma, B.J. Morgan, M. Body, C. Legein, W. Dachraoui, M. Giannini, A. Demortière, M. Salanne, F. Dardoize, H. Groult, O.J. Borkiewicz, K.W. Chapman, P. Strasser, D. Dambournet, Reversible magnesium and aluminium ions insertion in cation-deficient anatase TiO₂. Nat. Mater. 16 (2017) 1142–1148.
- [22] Y. Ai, S.C. Wu, K. Wang, T.Y. Yang, M. Liu, H.J. Liao, J. Sun, J.H. Chen, S.Y. Tang, D.C. Wu, T.Y. Su, Y.C. Wang, H.C. Chen, S. Zhang, W.W. Liu, Y.Z. Chen, L. Lee, J. H. He, Z.M. Wang, Y.L. Chueh, Three-dimensional molybdenum diselenide helical nanorod arrays for high-performance aluminum-ion batteries, ACS Nano 14 (2020) 8539–8550.
- [23] T. Leisegang, F. Meutzner, M. Zschornak, W. Münchgesang, R. Schmid, T. Nestler, R.A. Eremin, A.A. Kabanov, V.A. Blatov, D.C. Meyer, The aluminum-ion battery: a sustainable and seminal concept? Front. Chem. 7 (2019) 1–21.
 [24] M. Mao, C. Luo, T.P. Pollard, S. Hou, T. Gao, X. Fan, C. Cui, J. Yue, Y. Tong,
- [24] M. Mao, C. Luo, T.P. Pollard, S. Hou, T. Gao, X. Fan, C. Cui, J. Yue, Y. Tong, G. Yang, T. Deng, M. Zhang, J. Ma, L. Suo, O. Borodin, C. Wang, A. Pyrazine-Based, Polymer for Fast-Charge Batteries, Angew. Chem. - Int. Ed. 58 (2019) 17820–17826.
- [25] G.A. Elia, K. Marquardt, K. Hoeppner, S. Fantini, R. Lin, E. Knipping, W. Peters, J. F. Drillet, S. Passerini, R. Hahn, An overview and future perspectives of aluminum batteries, Adv. Mater. 28 (2016) 7564–7579.
- [26] H. Yang, H. Li, J. Li, Z. Sun, K. He, H.M. Cheng, F. Li, The rechargeable aluminum battery: opportunities and challenges, Angew. Chem. - Int. Ed. 58 (2019) 11978–11996.
- [27] J. Bitenc, N. Lindahl, A. Vizintin, M.E. Abdelhamid, R. Dominko, P. Johansson, Concept and electrochemical mechanism of an Al metal anode - organic cathode battery, Energy Storage Mater. 24 (2020) 379–383.
- [28] R. Cang, Y. Song, K. Ye, K. Zhu, J. Yan, J. Yin, G. Wang, D. Cao, Preparation of organic poly material as anode in aqueous aluminum-ion battery, J. Electroanal. Chem. 861 (2020) 1–8.

- [29] N.S. Hudak, Chloroaluminate-doped conducting polymers as positive electrodes in rechargeable aluminum batteries, J. Phys. Chem. C. 118 (2014) 5203–5215.
- [30] M. Walter, K.V. Kravchyk, C. Böfer, R. Widmer, M.V. Kovalenko, Polypyrenes as high-performance cathode materials for aluminum batteries, Adv. Mater. 30 (2018), 1705644.
- [31] N. Patil, A. Mavrandonakis, C. Jérôme, C. Detrembleur, J. Palma, R. Marcilla, Polymers bearing catechol pendants as universal hosts for aqueous rechargeable H +, Li-Ion, and Post-Li-ion (Mono-, Di-, and Trivalent) batteries, ACS Appl. Energy Mater. 2 (2019) 3035–3041.
- [32] D.J. Kim, D.J. Yoo, M.T. Otley, A. Prokofjevs, C. Pezzato, M. Owczarek, S.J. Lee, J. W. Choi, J.F. Stoddart, Rechargeable aluminium organic batteries, Nat. Energy 4 (2019) 51–59.
- [33] D.J. Yoo, M. Heeney, F. Glöcklhofer, J.W. Choi, Tetradiketone macrocycle for divalent aluminium ion batteries, Nat. Commun. 12 (2021) 1–9.
- [34] L. Zhang, Y. Qian, R. Feng, Y. Ding, X. Zu, C. Zhang, X. Guo, W. Wang, G. Yu, Reversible redox chemistry in azobenzene-based organic molecules for highcapacity and long-life nonaqueous redox flow batteries, Nat. Commun. 11 (2020) 3942
- [35] J. Li, M. Luo, Z. Ba, Z. Wang, L. Chen, Y. Li, M. Li, H.B. Li, J. Dong, X. Zhao, Q. Zhang, Hierarchical multicarbonyl polyimide architectures as promising anode active materials for high-performance lithium/sodium ion batteries, J. Mater. Chem. A 7 (2019) 19112–19119.
- [36] C. Luo, O. Borodin, X. Ji, S. Hou, K.J. Gaskell, X. Fan, J. Chen, T. Deng, R. Wang, J. Jiang, C. Wang, Azo compounds as a family of organic electrode materials for alkali-ion batteries, Proc. Natl. Acad. Sci. U. S. A. 115 (2018) 2004–2009.
- [37] H. Chen, H. Xu, S. Wang, T. Huang, J. Xi, S. Cai, F. Guo, Z. Xu, W. Gao, C. Gao, Ultrafast all-climate aluminum-graphene battery with quarter-million cycle life, Sci. Adv. 3 (2017) eaao723.
- [38] C. Luo, X. Ji, S. Hou, N. Eidson, X. Fan, Y. Liang, T. Deng, J. Jiang, C. Wang, Azo Compounds Derived from Electrochemical Reduction of Nitro Compounds for High Performance Li-Ion Batteries, Adv. Mater. 30 (2018), 1706498.
- [39] C. Chen, Y. Wen, X. Hu, X. Ji, M. Yan, L. Mai, P. Hu, B. Shan, Y. Huang, Na+intercalation pseudocapacitance in graphene-coupled titanium oxide enabling ultra-fast sodium storage and long-term cycling, Nat. Commun. 6 (2015) 6929.
- [40] I. Bouabibsa, S. Lamri, F. Sanchette, Structure, mechanical and tribological properties of Me-doped diamond-like carbon (DLC) (Me = Al, Ti, or Nb) hydrogenated amorphous carbon coatings, Coatings 8 (2018) 370.
- [41] S.W. Jung, M.C. Shin, M.A. Schweitz, J.M. Oh, S.M. Koo, Influence of gas annealing on sensitivity of aln/4h-sic-based temperature sensors, in: Materials (Basel), 14, 2021, pp. 1–7.
- [42] C.C. Lin, H.Y. Liou, S.Y. Chu, C.Y. Huang, C.S. Hong, Diverse resistive switching behaviors of AlN thin films with different orientations, CrystEngComm 20 (2018) 6230–6235.
- [43] L. Hu, Z. Xu, P. He, X. Wang, Z. Tian, H. Yuan, F. Yu, B. Dai, Zinc and Nitrogen-Doped Carbon In-Situ Wrapped ZnO Nanoparticles as a High-Activity Catalyst for Acetylene Acetoxylation. Catal. Lett. 150 (2020) 1155–1162.
- [44] D.Y. Osadchii, A.İ. Olivos-Suarez, A.V. Bavykina, J. Gascon, Revisiting nitrogen species in covalent triazine frameworks, Langmuir 33 (2017) 14278–14285.
- [45] Q. Wang, Q. Liu, Z. Wang, H. Liu, J. Bai, X-ray photoelectron spectroscopy investigation of nitrogen transformation in Chinese oil shales during pyrolysis, Oil Shale 34 (2017) 129–145.
- [46] X. Wang, S. Tan, X.Q. Yang, E. Hu, Pair distribution function analysis: fundamentals and application to battery materials, Chin. Phys. B 29 (2020), 028802.
- [47] C. Luo, E. Hu, K.J. Gaskell, X. Fan, T. Gao, C. Cui, S. Ghose, X.Q. Yang, C. Wang, A chemically stabilized sulfur cathode for lean electrolyte lithium sulfur batteries, Proc. Natl. Acad. Sci. U. S. A. 117 (2020) 14712–14720.
- [48] S.J.L. Billinge, The atomic pair distribution function: past and present, Z. Fur Krist. 219 (2004) 117–121.
- [49] A.P. Hammersley, S.O. Svensson, M. Hanfland, A.N. Fitch, D. Hausermann, Twodimensional detector software: From real detector to idealised image or two-theta scan, High Press. Res. 14 (2006) 235–248.
- [50] X. Qiu, J.W. Thompson, S.J.L. Billinge, PDFgetX2: a GUI-driven program to obtain the pair distribution function from X-ray powder diffraction data, J. Appl. Crystallogr. 37 (2004) 678.
- [51] B. Ravel, M. Newville, ATHENA, ARTEMIS, HEPHAESTUS: data analysis for X-ray absorption spectroscopy using IFEFFIT, J Synchrotron. Radiat. 12 (2005) 537–541.